



## Article

# Effect of Incidence Angle on Temperature Measurement of Solar Panel with Unmanned Aerial Vehicle-Based Thermal Infrared Camera

Hyeongil Shin <sup>1</sup>, Kourosch Khoshelham <sup>2</sup>, Kirim Lee <sup>3</sup>, Sejung Jung <sup>1</sup>, Dohoon Kim <sup>1</sup> and Wonhee Lee <sup>4,\*</sup>

<sup>1</sup> Department of Convergence and Fusion System Engineering, Kyungpook National University, Sangju 37224, Republic of Korea; gusrif6695@knu.ac.kr (H.S.); renai1226@knu.ac.kr (S.J.); dh8006@knu.ac.kr (D.K.)

<sup>2</sup> Department of Infrastructure Engineering, University of Melbourne, Melbourne 3010, Australia; k.khoshelham@unimelb.edu.au

<sup>3</sup> Research Institute of Artificial Intelligent Diagnosis Technology for Multi-Scale Organic and Inorganic Structure, Kyungpook National University, Sangju 37224, Republic of Korea; geolee@knu.ac.kr

<sup>4</sup> Department of Location-Based Information System, Kyungpook National University, Sangju 37224, Republic of Korea

\* Correspondence: wlee33@knu.ac.kr; Tel.: +82-54-530-1492

**Abstract:** This study utilizes Thermal Infrared (TIR) imaging technology to detect hotspots in photovoltaic (PV) modules of solar power plants. Unmanned aerial vehicle (UAV)-based TIR imagery is crucial for efficiently analyzing fault detection in solar power plants. This research explores optimal operational parameters for generating high-quality TIR images using UAV technology. In addition to existing variables such as humidity, emissivity, height, wind speed, irradiance, and ambient temperature, newly considered variables including the angle of incidence between the target object and the thermal infrared camera are analyzed for their impact on TIR images. Based on the solar power plant's tilt (20°) and the location coordinate data of the hotspot modules, the inner and outer products of the vectors were used to obtain the normal vector and angle of incidence of the solar power plant. It was discovered that the difference between measured TIR temperature data and Land Surface Temperature (LST) data varies with changes in the angle of incidence. The analysis presented in this study was conducted using multiple regression analysis to explore the relationships between dependent and independent variables. The Ordinary Least Squares (OLS) regression model employed was able to explain 63.6% of the variability in the dependent variable. Further, the use of the Condition Number (Cond. No.) and the Variance Inflation Factor (VIF) revealed that the multicollinearity among all variables was below 10, ensuring that the independence among variables was well-preserved while maintaining statistically significant correlations. Furthermore, a positive correlation was observed with the actual measured temperature values, while a negative correlation was observed between the TIR image data values and the angle of incidence. Moreover, it was found that an angle of incidence between 15° and 20° yields the closest similarity to LST temperature data. In conclusion, our research emphasizes the importance of adjusting the angle of incidence to 15–20° to enhance the accuracy of TIR imaging by mitigating overestimated TIR temperature values.

**Keywords:** multiple regression analysis; UAV; solar panel; TIR; incident angle; hotspot areas



**Citation:** Shin, H.; Khoshelham, K.; Lee, K.; Jung, S.; Kim, D.; Lee, W. Effect of Incidence Angle on Temperature Measurement of Solar Panel with Unmanned Aerial Vehicle-Based Thermal Infrared Camera. *Remote Sens.* **2024**, *16*, 1607. <https://doi.org/10.3390/rs16091607>

Academic Editors: Massimo Fabris, Giordano Teza and Arianna Pesci

Received: 4 April 2024

Revised: 23 April 2024

Accepted: 27 April 2024

Published: 30 April 2024



**Copyright:** © 2024 by the authors. Licensee MDPI, Basel, Switzerland. This article is an open access article distributed under the terms and conditions of the Creative Commons Attribution (CC BY) license (<https://creativecommons.org/licenses/by/4.0/>).

## 1. Introduction

### 1.1. Background

Considering the increasing interest in achieving carbon neutrality by 2050, the Ministry of Trade, Industry, and Energy in South Korea is planning a transition to make renewable energy the main energy source, aiming to reach a 25.8% share of renewable energy in total power generation by 2034, among which 22.2% will be contributed by renewable energy and 3.6% by new energy. According to the Renewable Energy Market Update released by

the International Energy Agency (IEA) [1], despite supply chain disruptions and delays in new construction caused by the COVID-19 pandemic, there was a notable 45% increase in the capacity of newly constructed renewable energy facilities in 2020 compared to the previous year.

According to the 2023 Renewable Energy Supply Statistics published by the Korea Energy Agency, solar energy constitutes a considerable portion of renewable energy, accounting for 38% of the total renewable energy production in 2021. Notably, a consistent increasing trend is observed for the new solar panel installation capacity in South Korea from 2017 to 2021, representing 87.9% of the total supply capacity of 4275 MW. However, solar photovoltaic (PV) modules have to operate in diverse outdoor environments, such as building rooftops, lakes, deserts, and mountains, with an expected operational lifespan of approximately 20–25 years [2]. Furthermore, natural wear and tear (seasonal debris, dust, discoloration, delamination, cracking humidity, and temperature) over time can result in an energy efficiency loss of 0.5–0.8% per year, according to the National Renewable Energy Laboratory (NREL) [3].

In solar PV-based power generation systems, one or more modules comprising multiple solar cell strings are connected in series or parallel [4]. This structural configuration poses a risk to the performance of the entire PV system and, consequently, to the performance of the respective module if abnormal signs appear in a single cell [5]. Therefore, preventing and maintaining solar panel faults are crucial challenges. The lifespan of solar modules can be categorized into two aspects: economic and functional lifespans. A solar module reaches its economic lifespan when it becomes economically attractive to enhance the efficiency of the solar module by replacing or upgrading it based on specific economic conditions in a solar system [6]. Meanwhile, a solar module is assumed to reach its functional lifespan when it ceases to produce electricity or it cannot guarantee electrical safety. Solar plant functional lifetime prediction models the progression of gradual degradation effects leading to a reduction in peak output. Early detection of deterioration effects that reduce maximum output is important to extend service life. Thus, the measured output yield of the module must not deteriorate by more than 8% from the initial output [7].

## 1.2. Prior Research

Common PV module inspection techniques for detecting anomalies in current solar power plants include TIR imaging, visual inspections, IV measurements, and periodic electroluminescence (EL) checks [6,8]. The temperature distribution of PV modules and cells installed in a PV system is expected to be uniform under normal operating conditions. However, defects in PV module can induce temperature differences ( $\Delta T$ ) between cells, making the accurate identification of hotspots a crucial concern for operations and maintenance teams, especially in high-temperature areas [9]. TIR imaging is a technology that detects long-wave (7–14  $\mu\text{m}$ ) radiation emitted from PV modules to identify hotspots [10,11]. Acciani et al. (2010) observed that hotspots exhibit a  $\Delta T$  of approximately 6–10  $^{\circ}\text{C}$  compared with adjacent normal cells [12].

Two main approaches for detecting hotspot areas using TIR imaging are UAVs and ground-based observations. Manual ground-based observations can be time-consuming, especially for assessing large-scale factories. However, UAV-based TIR imaging monitoring has been recognized as a cost-effective alternative due to its advantages such as a low cost, easy access, high observation frequency, and short inspection time [13,14]. Building on these advantages, the efficient analysis of UAV-based TIR images and their utilization as image processing tools to identify degraded PV modules have become standard practices [15–17].

Nevertheless, current standard practices in UAV-based TIR imaging research involve considering many external factors, as emphasized in previous studies [18–23] regarding various reliability issues related to PV module operation conditions and TIR imaging. Addressing these reliability issues requires careful consideration of weather conditions. Solar modules should be recorded under clear skies with solar irradiance exceeding 600  $\text{W}/\text{m}^2$  [24–28]. Additionally, recordings should be conducted in environments with

low wind speeds (<4 m/s) [17]. Capturing images at camera angles of less than  $60^\circ$  is also crucial [11,22]. Therefore, generating high-quality TIR images that can be efficiently analyzed is essential for accurately detecting defects using actual hotspot identification.

### 1.3. Need for Research

The primary aim of this study is to precisely analyze the initial hotspot regions in solar power plants, essential for effective defect detection and management. Directional Surface Thermal Anisotropy (STA), which influences LST inversion and applications, has been studied in several works [29–31]. Historically, most studies using UAV data have overlooked the STA of LST emissions. Like satellite acquisitions, UAV collections are ideally suited for capturing TIR images simultaneously across entire scenes, yet this comes at the cost of maintaining a wide Field of View (FOV), thus necessitating strategies to correct for STA. Despite the inevitable angular effects in thermal imagery necessitating corrections, the accompanying meteorological conditions make comparisons easier. Furthermore, spatial resolution remains a significant concern in the current discourse on TIR angular normalization. Utilizing UAV-based sensors enables pixel acquisition at spatial resolutions under one meter. When STA occurs, the surface structure significantly impacts Brightness Temperature (BT) measurements, with considerable variability observed even among adjacent pixels within the same surface [32]. To date, investigations into fine TIR data from UAVs related to STA have lacked in-depth analysis and thorough interpretation. Additionally, studies analyzing the impact of existing angles have been conducted based on the maximum observation zenith angle for the ground [33], aircraft [29], or satellite [34,35]. However, considering the superior spatial resolution provided by UAV-based systems compared to traditional methods, relying solely on zenith angles for data collection can be problematic. Even at consistent zenith angles, the direction of objects can lead to occurrences of STA, thereby compromising the accuracy of data collection. To overcome this issue, it is crucial to consider the incidence angles relative to the thermal sensor and the target during the acquisition of TIR data. This approach ensures a more precise and reliable dataset by accommodating the varying impacts of STA based on the orientation of objects relative to the sensor's position.

To address these issues, this research utilizes UAV-based technology to generate high-quality TIR images while considering incidence angles during data acquisition. The relationship between TIR images and incidence angles requires reliance on two theoretical foundations: Planck's Law and Lambert's cosine law. Planck's Law quantifies the spectral distribution of electromagnetic radiation emitted by a black body in thermodynamic equilibrium, represented as a specific function that varies with the wavelength and temperature of the radiated energy (Figure 1). This law demonstrates that as the temperature of a radiator increases, the peak of the emitted radiation shifts to shorter wavelengths, i.e., higher energy regions, and the total amount of radiation increases proportionally to the fourth power of the temperature. Based on these phenomena, thermal infrared cameras can detect different wavelengths and distinguish between high-temperature and low-temperature objects, displaying them on the image. Thus, it is feasible to differentiate between normal and abnormal modules in solar power plants based on these phenomena, significantly contributing to the operation and maintenance of solar power facilities. Moreover, evaluating the incidence angle as a critical variable is based on the fundamental principles of Lambert's cosine law. Lambert's cosine law describes the optical principle that the intensity of light emitted decreases in proportion to the cosine of the observation angle as incident light reaches an ideal scattering surface. This implies that the intensity of observed light diminishes as the angle from the light source increases, with the maximum energy amount measured when the emission area is perpendicular ( $90^\circ$ ) to the observer (Figure 2). As the incidence angle increases, the measured radiative energy decreases according to the cosine function properties, with the cosine value being 1 at a  $0^\circ$  angle (normal direction), and the incidence angle ranging from 0 to  $90^\circ$ . Lambert's law, assuming uniform scattering of light by a Lambertian surface, plays a crucial role in accurately measuring and predicting radi-

ance in remote sensing. By applying both Planck's Law of thermal emission and Lambert's cosine law, it is anticipated that changes in radiative energy due to incidence angles could significantly impact the quality of TIR images. This theoretical foundation is essential for understanding and determining the parameters necessary to optimize TIR imagery. In the next section, we will explain research methods that are different from existing studies based on these theories.

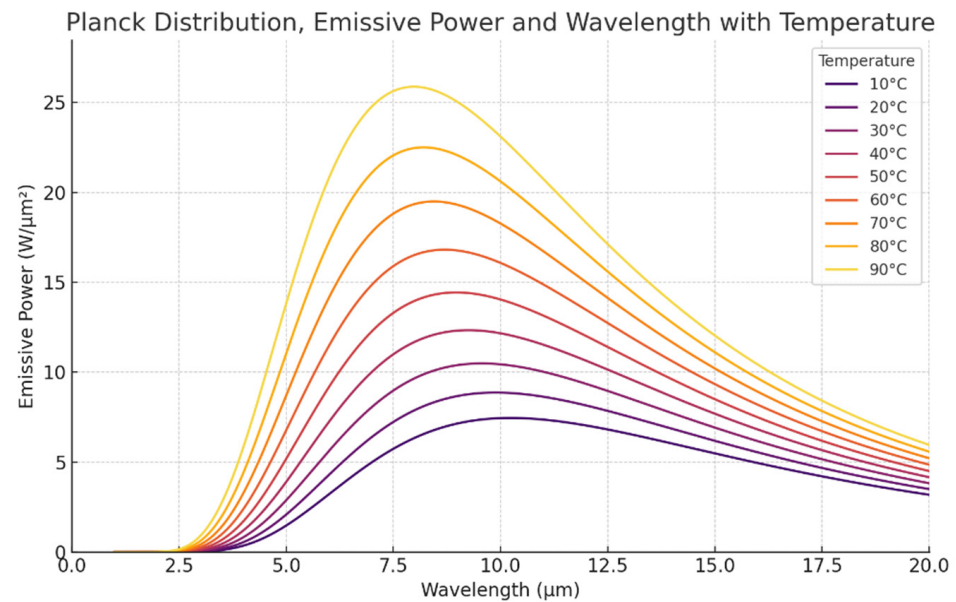


Figure 1. Planck wavelength distribution curve.

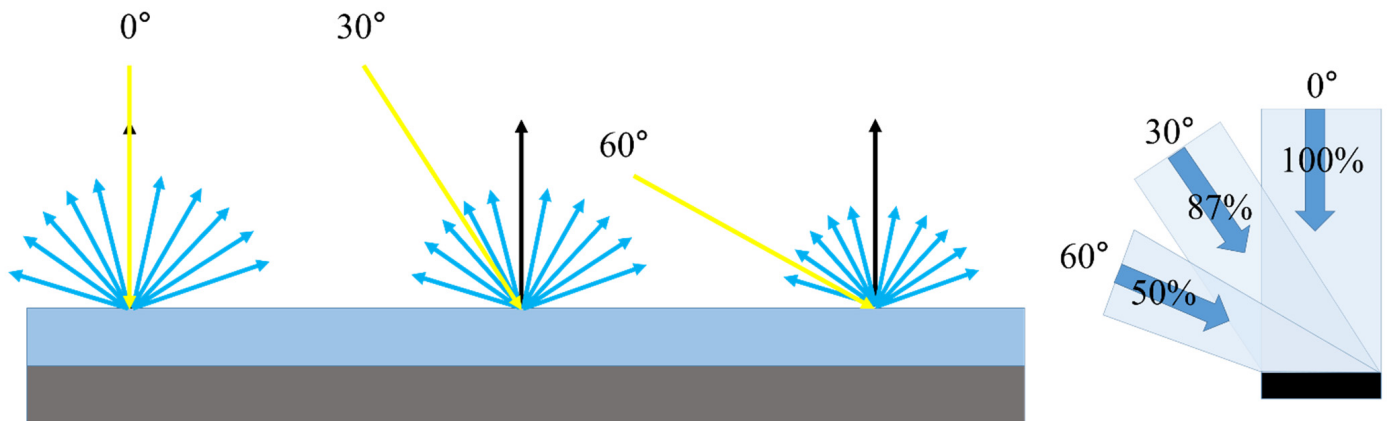


Figure 2. Lambert's cosine law.

## 2. Materials and Methods

### 2.1. Study Equipment

This study employed a UAV and a TIR camera to acquire TIR images using a remote sensing system. The UAV utilized was the DJI Matrice 300 RTK, and the TIR camera utilized was the DJI Zenmuse H20T. The Matrice 300 RTK's specifications include a maximum flight altitude of 5000 m, a maximum speed of 23 m/s in calm conditions, and the ability to fly for up to 55 min with no wind. The weight of the UAV (DJI Matrice 300 RTK), including propellers and batteries, is approximately 6.3 kg, increasing to approximately 7.1 kg when equipped with the Zenmuse H20T. The Matrice 300 RTK is a rotorcraft powered by four propellers (Table 1).

The Zenmuse H20T utilizes a non-cooled Vanadium Oxide (VOx) microbolometer sensor with a focal length of 13.5 mm, a 40.6° display field of view (DFOV), and a resolution of 640 × 512 pixels. The sensor features a pixel pitch size of 12 μm and a spectral range of 8–14 μm. The temperature camera’s target temperature range is configured as −40–150 °C (high gain) and −40–550 °C (low gain). The Zenmuse H20T’s vibration angle range is ±0.01°, precisely minimizing angle changes due to the drone’s vibrations. The methods for measuring temperature include spot metering and area measurement, ensuring a temperature accuracy of either ±2 °C or ±2% of the measured temperature in Celsius, choosing whichever of these two values is greater, to account for normal surface temperature variations [36].

**Table 1.** UAV, TIR camera, and laser thermometer specifications.

UAV		Thermal Infrared Camera		Laser Thermometer	
Weight	6300 g	Resolution	640 × 512	Temperature range	−50–380 °C (−58–716 °F)
Flight altitude	Max: 5000 m	Pixel size	12 μm	Accuracy	1.5% or 1.5 °C
Flight time	Max: 55 min	DFOV	40.6°	Resolution	0.1 °C
Speed	Max: 23 m/s	Focal length	13.5 mm	Wavelength	8–14 μm
Maximum wind resistance	15 m/s	Scene range	−40–150° (High gain) −40–550° (Low gain)	Emissivity	0.95

For the measurement of on-site LST, the laser thermometer model GM 320 was utilized. This thermometer is capable of measuring temperatures within a broad range of −50 °C to 400 °C, providing results with high precision. The accuracy of the temperature readings is expressed as either ±1.5% of the measured temperature in Celsius or ±1.5 °C, with the protocol to adopt whichever of these two values is greater [37]. To compare temperature values at precise locations during ground LST acquisition, position coordinates were obtained by global navigation satellite system (GNSS) surveying utilizing the virtual reference station (VRS) method to obtain position coordinates. Additionally, ground control points (GCPs) required for temperature orthophoto production were acquired. The GNSS surveying equipment utilized was Trimble’s R8s, featuring 440 channels and VRS measurement accuracies of 8 mm + 0.5 ppm RMS in the horizontal direction and 15 mm + 0.5 ppm RMS in the vertical direction [38].

## 2.2. Study Area

In this study, a solar panel situated on the rooftop of Building 10 at the Sangju Campus of Kyungpook National University was designated as the research area for the precise collection of temperature data within the suspected hotspot region, indicative of a potential malfunction in solar power generation. Several challenges arose in locating a solar panel with an authentic hotspot area, prompting the decision to substitute the hotspot region with 20 × 20 cm<sup>2</sup> black silicone rubber pieces. Solar cells are made of silicon material. The method of fixing solar panels involves attaching glass to the solar cells. In this study, it was determined that the main body of the solar panel is the solar cells rather than glass. Since the cells are made of silicon, similar environmental conditions were simulated using silicone rubber for data acquisition. Glass, being heavy and reflecting a lot of light, was considered unsuitable for creating arbitrary hotspot module areas. The reason for selecting 20 × 20 cm<sup>2</sup> is to minimize the impact on surrounding solar cells by aligning it with the dimensions of the solar cells.

### 2.3. Data Acquisition and Processing

In Section 2.3, titled “Data Acquisition and Processing”, we acquire the following data: LST values, UAV-based TIR temperature values, and WGS84 coordinates using the GCPs and feature points from the orthophoto, as illustrated in Figure 3. Subsequently, we calculate the angle of incidence based on the acquired data and demonstrate its correlation through multiple regression analysis. In the Results and Discussion Sections, we compare and analyze the variations in TIR data attributed to the angle of incidence and explore the correlation between the angle of incidence and TIR data. Furthermore, we identify the range of incident angles conducive to obtaining accurate TIR data through comparative analysis. In the following sections, we discuss the research methods, results, and how these results differ from previous studies.

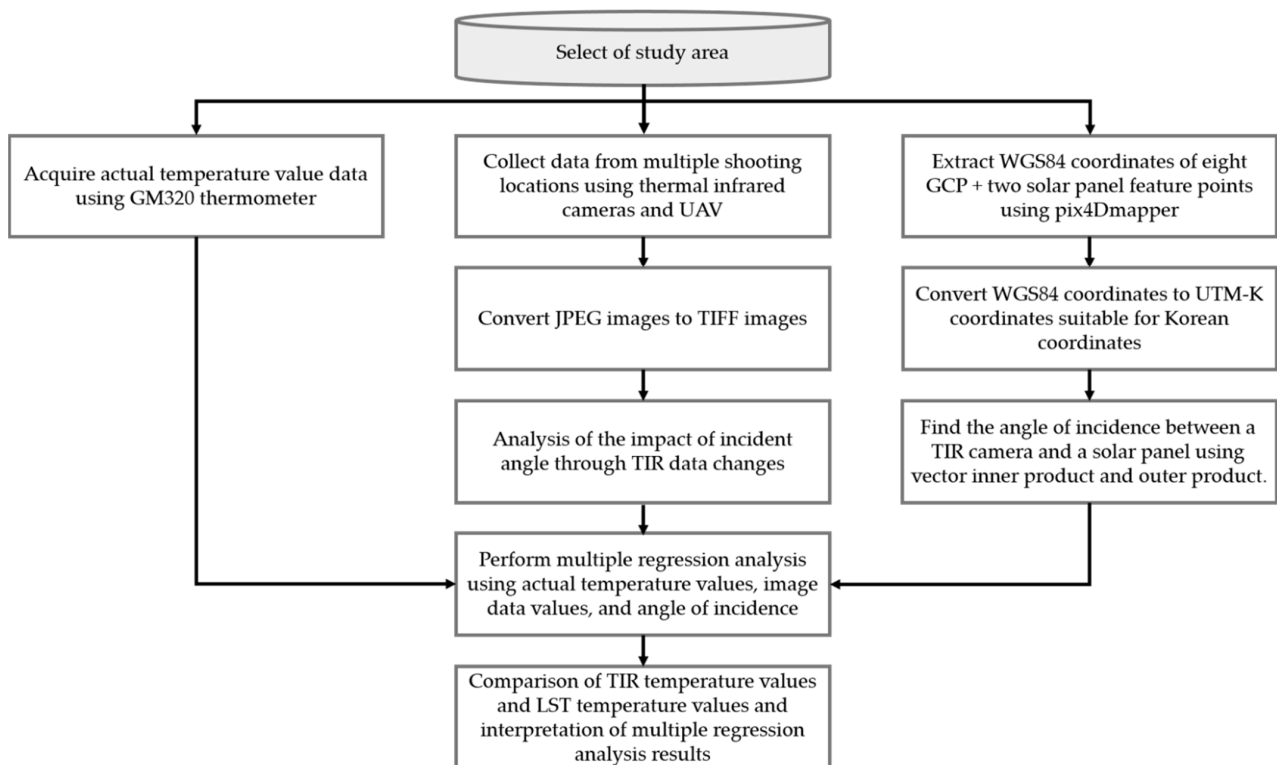


**Figure 3.** Overall study flow chart.

#### 2.3.1. Temperature Data Acquisition

In this study, we investigated the correlation between the incidence angle and TIR data generated by a UAV-based TIR camera. Optimal meteorological conditions for TIR data collection were selected on the basis of meteorological data from the National Meteorological Administration. Specifically, days with solar radiation exceeding  $600 \text{ W/m}^2$  and wind speeds below  $4 \text{ m/s}$  were selected. For the TIR data and LST assessments, we positioned six segments of silicone rubber, sequentially numbered from 1–6, upon the solar module. Data capture was methodically executed by designating the image’s centroid as the principal points, identified as points a, b, and c (Figure 4). The average temperature of eight adjacent regular module regions was measured six times each, in addition to the six measurements that were performed for each randomly selected hotspot areas (Figure 4). Additionally, a temperature difference ( $\Delta T$ ) within the range of  $10\text{--}20 \text{ }^\circ\text{C}$  was considered as a potential hotspot area exceeding the maximum allowable limit for effective power loss [20]. Thus, data collection commenced when  $\Delta T$ , relative to the normal module temperature, was within the  $10\text{--}20 \text{ }^\circ\text{C}$  range (Table 2). The flight lasted approximately 10 min from 3:24 PM to 3:34 PM on 11 October 2023, and a total of 179 images were acquired. During the 10 min recording process,  $\Delta T$  increased by approximately  $2 \text{ }^\circ\text{C}$ . Key environmental variables considered

for the conversion of the acquired data into temperature values included distance from target object, ambient humidity, and emissivity. The surrounding humidity was measured to be 48% based on the information from the Korea Meteorological Administration, and the emissivity of the target surface was set to 0.9, according to the infrared thermometer emissivity table. Furthermore, to process the LST data for comparison with TIR data, the originally set emissivity of 0.95 was adjusted to 0.9 (Equation (1)). This conversion is grounded in Planck's Law and the Stefan–Boltzmann Law, which describe that radiative energy is proportional to the fourth power of temperature. In this framework,  $T_2$  represents the adjusted new temperature value, whereas  $T_1$  is the temperature measured with the original emissivity  $\epsilon_1$ , and the new emissivity is set at  $\epsilon_2$ . Additionally, the altitude of the UAV ( $h$ ) is set at 50 m, the solar panel angle is positioned at  $20^\circ$ , the maximum distance between the panel and UAV is 70 m, and the dimensions of the panel are 1.74 m in width and 1.042 m in height. UAV-based TIR data were collected from 18 different locations, each at an altitude of 50 m from the UAV takeoff point (Figure 5). In the R code used to convert the temperature value of the thermal infrared camera, the maximum distance was set to 25 m, and distances exceeding 25 m were fixed at 25 m. Hence, the distance from target object was uniformly set to 25 m. The reason for collecting data from 18 locations is to fix the thermal infrared camera angle to  $90\text{--}40^\circ$  based on the solar panel to determine changes in the incident angle depending on the location and to examine changes in image data value.

$$T_2 = T_1 \left( \frac{\epsilon_1}{\epsilon_2} \right)^{\frac{1}{4}} \quad (1)$$

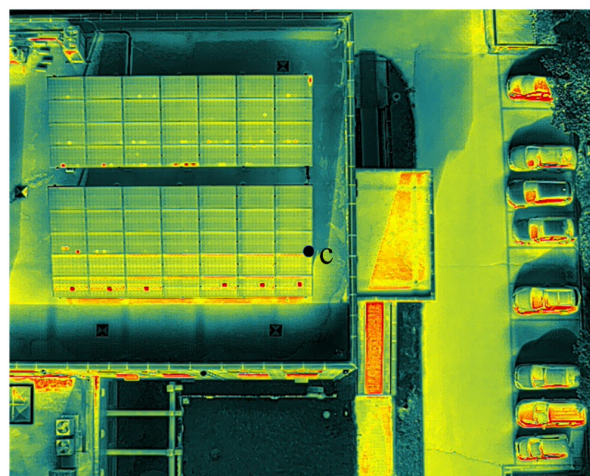
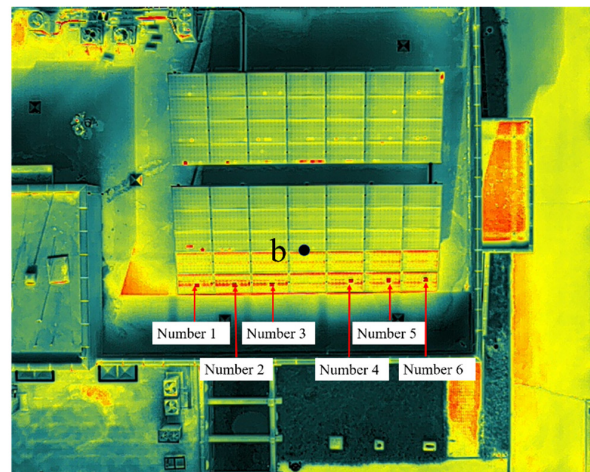
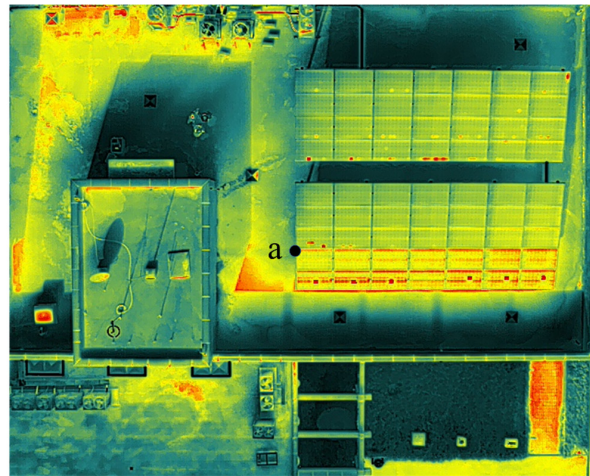
**Table 2.** LST value.

Number	Hotspot Area Temperature	Normal Module Temperature
1	46.46 °C	34.54 °C
2	44.2 °C	35.61 °C
3	48.4 °C	35.41 °C
4	52.78 °C	35.5 °C
5	53.76 °C	36.44 °C
6	47.66 °C	36.27 °C

### 2.3.2. GPS Data Acquisition

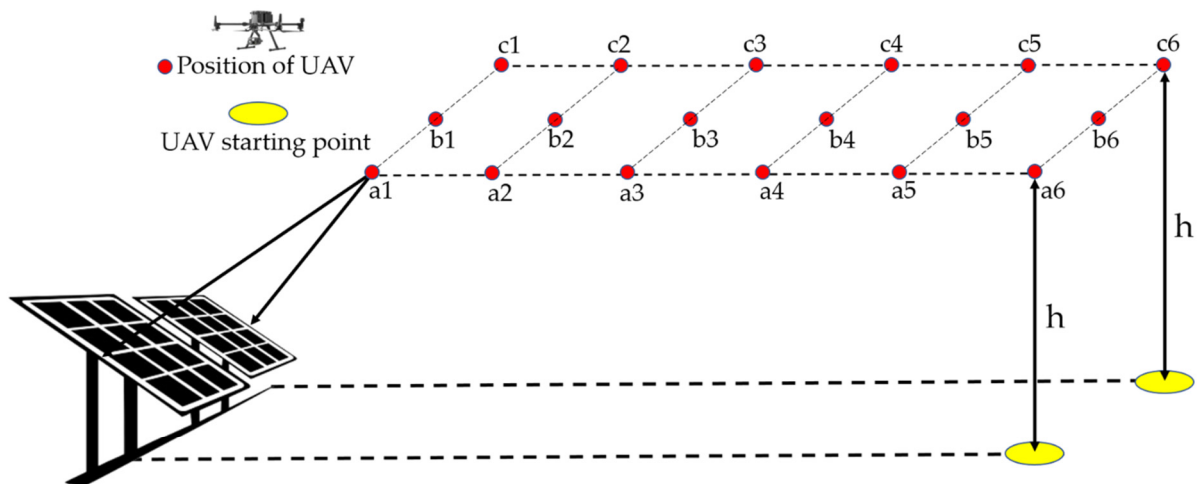
Determining the incidence angle between the UAV-based thermal infrared camera and hotspot area requires the extraction of the exact coordinates of the study area. The GCPs were established using eight anti-aircraft signs to obtain accurate coordinate values, and survey data were acquired using Trimble's R8s GPS equipment. Among the Network Real-Time Kinematic (RTK) methods, the Virtual Reference Station (VRS) approach was selected as the survey method in this study. Conventionally, in GPS surveying, receiver positions are determined based on the signals received from a reference station. However, in the VRS method, a virtual reference station is generated utilizing observation data and a precise position calculation algorithm from multiple distributed real GPS base stations [39]. This virtual reference station corrects errors in GPS signals and provides accurate location information considering the geometric relationships between these base stations. The transmitted information is then integrated with data from three continuous operation reference stations to eliminate systematic errors related to the ionosphere and convection layer. During the VRS survey, GPS signals were received, including L1C/A, L1C, L2C, and L5 signals. Additionally, signals from GLONASS, SBAS, and Galileo satellites were used, and the total number of GPS satellites used in this study was in the range of 13–16. Observations were made at 1 s intervals for more than 10 s, and measurements were restricted to values within 0.05 m horizontally and 0.10 m vertically based on the allowable precision regulations. Applying the data obtained using the same method

to Pix4Dmapper, we designate eight GCP positions installed in the study area and two white areas representing boundaries between solar modules as key points to obtain GPS coordinates in WGS84 coordinates (Figure 6), for use in the paper.



●(a,b,c) : Thermal infrared camera principal position  
Number1~6 : Actual locations of hotspot area

**Figure 4.** Actual locations of the hotspot area and TIR camera principal points.



h : Observation height, flying height of UAV  
 a1~a6 : Horizontal angular position of the UAV relative to the left side of the module area (thick white line)  
 b1~b6 : Horizontal angular position of the UAV relative to the center side of the module area (thick white line)  
 c1~c6 : Horizontal angular position of the UAV relative to the right side of the module area (thick white line)

Figure 5. Data acquisition method.



● Border between solar panels (white area)

Figure 6. Orthophotos of the study area.

#### 2.4. Incidence Angle Data Acquisition

Accurate determination of the incidence angle ( $\theta$ ) depends on acquiring precise coordinates: the hotspot area on the solar panel (points A and B), the principal point of the thermal infrared camera (point C), and the position of the UAV equipped with the TIR camera (point D). These coordinates were obtained using Pix4Dmapper for points A, B, and C, and from UAV navigation data for point D. Initially in the WGS84 coordinate system, they were converted to the UTM-K system, which is tailored for South Korea, to correct any discrepancies caused by differences in coordinate systems.

To calculate  $\theta$ , vectors  $\vec{v}_{AB}$  and  $\vec{v}_{AC}$  are first constructed using the coordinates on the photovoltaic panel (A, B, C). The normal vector  $\vec{n}$  is ascertained through the cross product of  $\vec{v}_{AB}$  and  $\vec{v}_{AC}$ , which ensures it is orthogonal to the panel surface (Equation (2)). A crucial step is assessing the z-component of the normal vector, denoted as  $\gamma$ , to confirm that  $\theta$  is within the desired range of  $0\text{--}90^\circ$ . Given that the UAV's altitude is higher than that of the solar panels, converting a negative  $\gamma$  to a positive one through the application of an inverse vector is necessary to maintain the accuracy of the angular measurements.

Next, vector  $\vec{v}_{AD}$  is computed using the coordinates of A (hotspot) and D (UAV location). The incidence angle,  $\theta$ , is then accurately determined by the vectorial relationship between  $\vec{v}_{AD}$  and  $\vec{n}$ , as outlined in Equations (3)–(7). This method meticulously details the spatial relationship between the UAV's altitude and the angular orientation of the solar panel, enabling precise calculation of  $\theta$ . The precision of this calculation is crucial for interpreting data in photovoltaic performance studies and provides the necessary mathematical framework for assessing the angle of incidence during TIR data acquisition (Figure 7).

$$\vec{n} = \vec{v}_{AB} \times \vec{v}_{AC} \quad (2)$$

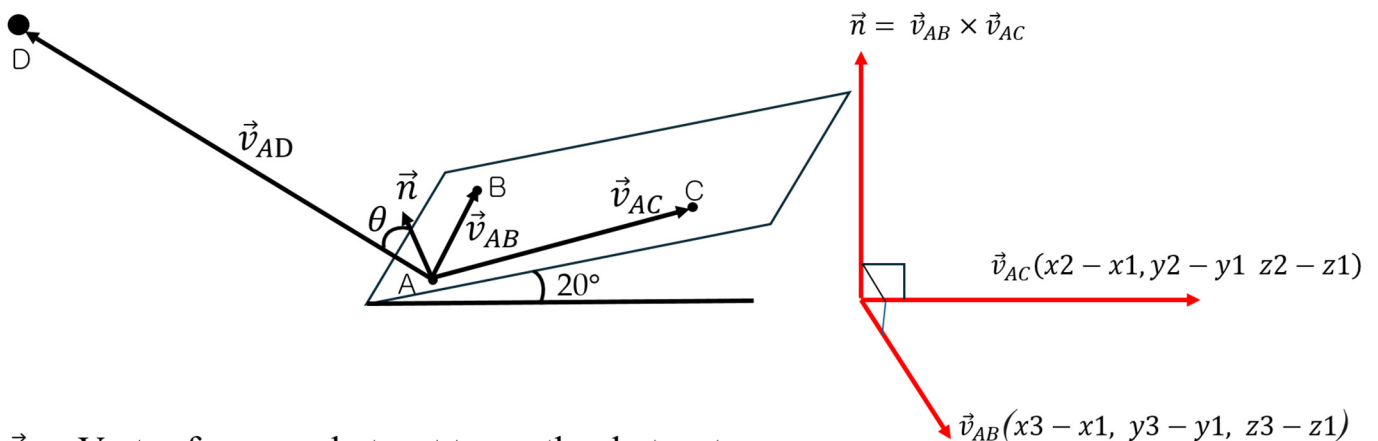
$$\vec{n} = (\alpha, \beta, \gamma) \quad (3)$$

$$\vec{v}_{AD} = (x_4 - x_1, y_4 - y_1, z_4 - z_1) \quad (4)$$

$$\vec{n} \cdot \vec{v}_{AD} = |\vec{n}| |\vec{v}_{AD}| \cos \theta \quad (5)$$

$$\cos \theta = \frac{\vec{n} \cdot \vec{v}_{AD}}{|\vec{n}| |\vec{v}_{AD}|} \quad (6)$$

$$\theta = \cos^{-1} \left( \frac{\vec{n} \cdot \vec{v}_{AD}}{|\vec{n}| |\vec{v}_{AD}|} \right) \quad (7)$$



$\vec{v}_{AB}$ : Vector from one hotspot to another hotspot

$\vec{v}_{AC}$ : Vector from hotspot to camera principal point

$\vec{v}_{AD}$ : Vector from hotspot to camera

$\theta$ : Angle of incidence

$\vec{n}$ : Normal vector

**Figure 7.** Information required to determine the incidence angle.

### 2.5. Multiple Regression Analysis

To assess how the angle of incidence between a UAV-based TIR camera and the hotspot region affects the values in TIR image data, it is imperative to choose an appropriate regres-

sion analysis method for analyzing the key variables involved. In this study, the principal variables include the actual temperature of the hotspot area, the temperature values derived from the TIR images of the hotspot, and the incidence angle. Firstly, it is vital to establish the roles of the dependent and independent variables in the analysis. The dependent variable, which is the primary focus of this study, is the temperature of the hotspots as recorded in the TIR images. The independent variables are identified as the actual measured temperature of the hotspot and the incidence angle. Given that the temperature value is a continuous dependent variable and there are multiple continuous independent variables, multiple regression analysis is selected as the most suitable statistical method. This approach will enable the exploration of the relationships between the incidence angle, actual temperature, and the temperature recorded in the TIR images.

Before conducting the multiple regression analysis, it is essential to standardize both dependent and independent variables. The use of the StandardScaler, a standard scaling methodology, ensures that the mean of each feature is adjusted to zero and the variance to one, guaranteeing that all features are on the same scale. This standardization ensures uniformity across all features, simplifying the interpretation of relationships among the variables and enhancing the clarity of data interactions. Moreover, standardization plays a crucial role in mitigating the influence of outliers, which enhances the accuracy of the regression analysis and supports more reliable statistical inferences.

### 3. Results

#### 3.1. TIR-Measured Temperature Results

This study underscores the significance of conducting regular inspections to promptly identify faults in solar panels, particularly emphasizing techniques for accurately detecting hotspot areas. In experiments, the temperature differential between hotspot modules and standard modules was established at approximately 10 °C. Measurements taken using TIR technology at various camera focuses and UAV positions revealed temperature disparities ranging from 1 to 10 °C for hotspot modules (Table 3), while standard modules showed temperature variations from 1 to 3 °C (Table 4). These findings indicate that temperature fluctuations are more pronounced in hotter objects than in cooler ones, predominantly due to shifts in the angle of incidence between the hotspot zones and the TIR cameras, even amidst stable external environmental conditions.

When using TIR cameras for hotspot detection, the sensitivity to temperature differences between normal and hotspot areas is inevitable since the detection process relies solely on these temperature variations. The commonly used method for acquiring UAV-based TIR data involves automated vertical flights over solar power installations, consistent with the techniques employed at locations a1, b1, and c1. At these points, the difference between LST values and TIR temperature readings of hotspot modules varied approximately from 9 to 13 °C. Conversely, the temperature differences noted in standard module TIR readings were around 8 °C. Although this widely used method can identify hotspot areas, a more detailed and accurate analysis is required to find hotspot areas with higher precision. This necessitates a meticulous examination of temperature values recorded at 18 UAV positions covering various angles of incidence.

In particular, the highest TIR temperature measurements noted at a2, b2, and c2 were about 2 °C higher on average than those obtained through conventional methods, with standard modules registering approximately 1 °C higher. On the other hand, the lowest TIR temperature readings for hotspot modules at a6, b6, and c6 were about 7 °C lower, while those for standard modules were around 2 °C lower. This analysis indicates that TIR temperature readings tend to decrease as the angle of incidence increases, highlighting a critical aspect of TIR data interpretation in relation to photovoltaic performance assessments.

**Table 3.** Hotspot module temperature values of the TIR images.

Position of UAV	Number 1 Temperature	Number 2 Temperature	Number 3 Temperature	Number 4 Temperature	Number 5 Temperature	Number 6 Temperature
a1	56.79 °C	53.94 °C	59.87 °C	62.86 °C	63.31 °C	60.84 °C
a2	58.86 °C	55.66 °C	60.08 °C	64.06 °C	65.94 °C	62.58 °C
a3	56.91 °C	53.64 °C	60.98 °C	63.28 °C	64.06 °C	59.36 °C
a4	54.58 °C	52.07 °C	59.39 °C	61.34 °C	61.97 °C	62.5 °C
a5	52.98 °C	51.5 °C	57.28 °C	59.4 °C	59.45 °C	57.43 °C
a6	50.71 °C	49.57 °C	54.66 °C	56.50 °C	56.84 °C	50.19 °C
b1	57.63 °C	53.89 °C	58.18 °C	63.68 °C	63.92 °C	56.04 °C
b2	58.52 °C	54.85 °C	61.04 °C	63.63 °C	63.78 °C	56.33 °C
b3	56.93 °C	49.60 °C	59.03 °C	63.38 °C	64.26 °C	58.99 °C
b4	55.54 °C	52.41 °C	59.64 °C	61.83 °C	62.92 °C	63.06 °C
b5	54.17 °C	51.65 °C	57.19 °C	59.91 °C	60.04 °C	57.17 °C
b6	52.13 °C	48.98 °C	53.30 °C	56.72 °C	57.71 °C	53.29 °C
c1	56.58 °C	53.91 °C	57.27 °C	63.77 °C	64.64 °C	58.82 °C
c2	58.73 °C	55.65 °C	60.66 °C	64.32 °C	65.29 °C	57.54 °C
c3	56.82 °C	59.56 °C	53.50 °C	63.81 °C	62.78 °C	64.16 °C
c4	57.18 °C	54.35 °C	60.79 °C	63.78 °C	65.54 °C	60.38 °C
c5	52.93 °C	50.97 °C	55.45 °C	59.29 °C	60.69 °C	58.92 °C
c6	49.23 °C	48.16 °C	51.66 °C	53.41 °C	54.29 °C	49.74 °C

**Table 4.** Normal module temperature values of the TIR images.

Position of UAV	Ambient Temperature Value of Number 1	Ambient Temperature Value of Number 2	Ambient Temperature Value of Number 3	Ambient Temperature Value of Number 4	Ambient Temperature Value of Number 5	Ambient Temperature Value of Number 6
a1	43.21 °C	44.16 °C	44.13 °C	44.45 °C	44.41 °C	44.55 °C
a2	44.95 °C	45.86 °C	45.74 °C	46.03 °C	46.16 °C	46.65 °C
a3	43.98 °C	45.62 °C	45.25 °C	44.93 °C	45.02 °C	44.67 °C
a4	43.99 °C	45.49 °C	46.19 °C	45.27 °C	44.92 °C	45.43 °C
a5	41.84 °C	43.94 °C	44.29 °C	42.33 °C	43.09 °C	42.11 °C
a6	40.83 °C	42.24 °C	42.29 °C	41.03 °C	40.33 °C	40.06 °C
b1	43.81 °C	44.55 °C	44.7 °C	44.73 °C	44.47 °C	44.45 °C
b2	44.97 °C	45.57 °C	45.3 °C	45.48 °C	45.13 °C	45.33 °C
b3	43.86 °C	45.01 °C	44.7 °C	44.16 °C	43.96 °C	44 °C
b4	44.2 °C	45.87 °C	46.07 °C	45.6 °C	46.49 °C	45.68 °C
b5	41.71 °C	43.04 °C	43.09 °C	42.58 °C	41.86 °C	42.13 °C
b6	42.15 °C	42.57 °C	42.67 °C	41.68 °C	41.12 °C	40.55 °C
c1	43.91 °C	44.55 °C	44.42 °C	44.65 °C	44.29 °C	44.23 °C
c2	43.8 °C	44.59 °C	44.29 °C	44.21 °C	43.58 °C	44.08 °C
c3	44 °C	45.01 °C	44.87 °C	44.2 °C	44.35 °C	43.55 °C
c4	44.3 °C	45.89 °C	45.09 °C	45.21 °C	45.08 °C	44.27 °C
c5	42.77 °C	44.29 °C	43.41 °C	42.68 °C	41.77 °C	41.6 °C
c6	41.41 °C	42.13 °C	42.57 °C	41.02 °C	40.6 °C	39.93 °C

### 3.2. Multiple Regression Analysis Results

Prior to quantitatively illustrating the phenomenon wherein the TIR temperature value decreases with an increase in the angle of incidence through multiple regression analysis, this study thoroughly examined the significance and reliability of the multiple regression analysis technique.

The R-squared value indicates that approximately 63.6% of the variance in the image value can be explained by the independent variables. The adjusted R-squared, considering the number of predictors, is 62.9%, suggesting a solid fit. A high F-statistic value of 91.60 indicates that the model significantly outperforms a baseline model with no independent variables, implying a meaningful linear relationship between independent and dependent variables. A significantly low  $p$ -value ( $<0.05$ ) indicates high confidence in rejecting the null hypothesis and supports the model's predictive capability. These metrics evaluate the model's fit and complexity. Lower AIC and BIC values are preferred, indicating a better balance between model complexity and fit. This represents the balance between the number of observations and independent variables. Df Residuals and Df Model indicate the flexibility and complexity of the model, respectively. The Cond. No. value indicates the degree of multicollinearity, with a higher value suggesting stronger correlations among variables (Table 5). VIF values  $> 10$ – $20$  indicate multicollinearity, but in this case, VIF values are low ( $<1.006$ ), confirming the absence of multicollinearity (Table 6).

**Table 5.** OLS regression results.

Item	Value	Description
Dependent Variable	Image value	Variable being predicted or explained in the analysis
R-squared	0.636	Proportion of variance in the dependent variable explained by the model (63.6%)
Adjusted R-squared	0.629	Adjusted R-squared considering the number of predictors
F-statistic	91.60	Overall fit of the model
Prob (F-statistic)	$9.51 \times 10^{-24}$	$p$ -value for the F-statistic, assessing the significance of the model
Log-Likelihood	−98.721	Log-likelihood of the model fit
AIC	203.4	Akaike Information Criterion, a measure of model quality
BIC	211.5	Bayesian Information Criterion, a measure of model quality
Df Residuals	105	Degrees of freedom of residuals
Df Model	2	Number of predictors in the model
Omnibus	0.827	Omnibus test statistic for the normality of residuals
Prob (Omnibus)	0.661	$p$ -value of the Omnibus test
Durbin–Watson	1.321	Durbin–Watson statistic for testing the independence of residuals
Jarque–Bera (JB)	0.909	Jarque–Bera test statistic for the normality of residuals
Skew	0.111	Measurement of the asymmetry (skewness) of residuals
Kurtosis	2.609	Measurement of the peak of residuals
Prob(JB)	0.635	$p$ -value of the Jarque–Bera test
Cond. No.	1.08	Condition number indicating the degree of multicollinearity

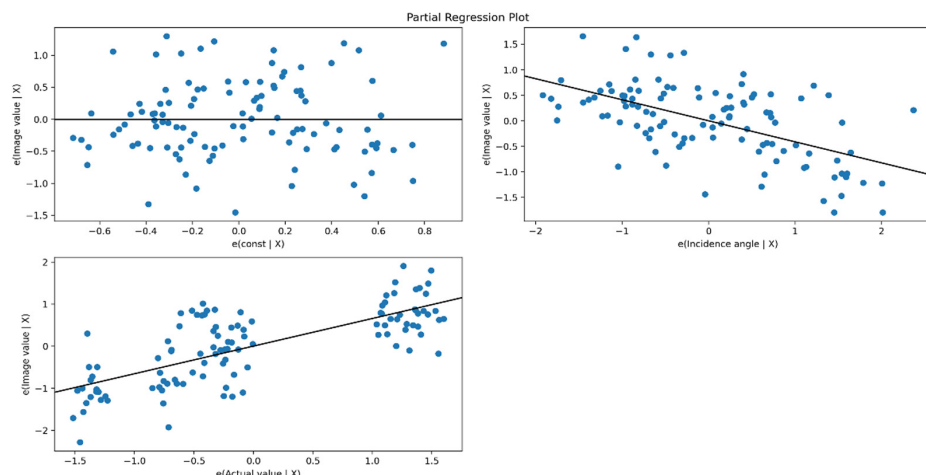
**Table 6.** VIF value to check multicollinearity.

Features	VIF Factor
Constant	1.0
Incidence angle	1.0056909218225500
Actual value	1.0056909218225500

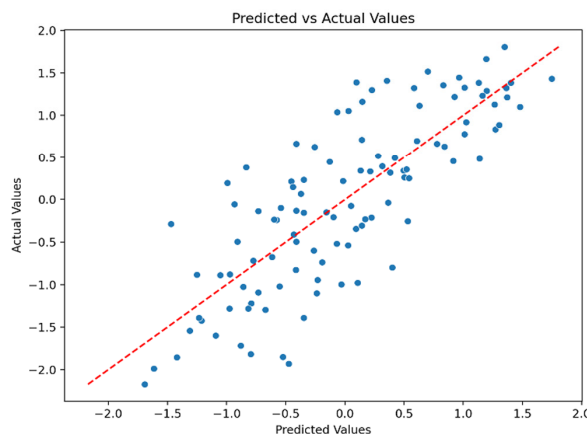
In this study, the numbers and values presented in Tables 5 and 6 indicate that the results of the multiple regression analysis are meaningful. Collectively, the regression statistics (Table 7) indicate that the regression coefficients represent changes in the dependent variable corresponding to a single-unit change in the independent variables, while all other variables remain constant. The negative coefficient of the incidence angle ( $-0.4004$ ) indicates an inverse relationship with the dependent variable, implying that the value of the dependent variable tends to decrease with the increasing incidence angle. Conversely, the positive coefficient for the actual value ( $0.6600$ ) suggests a direct relationship, indicating that an increase in the actual value correlates with an increase in the dependent variable (Figure 8). The standard error measures the accuracy with which these coefficients are estimated. A low standard error, as in this case ( $0.059$ ), implies that the estimated regression coefficients are likely to be close to the true population values, indicating high precision in the estimation.

**Table 7.** Statistical analysis results of the regression analysis.

Features	Coef	Std Err	t	P >  t	[0.025	0.975]
Const	$3.708 \times 10^{-12}$	0.059	$6.29 \times 10^{-11}$	1.000	-0.117	0.117
Incidence angle	-0.4004	0.059	-6.778	0.000	-0.518	-0.283
Actual value	0.6600	0.059	11.173	0.000	0.543	0.777



(a)



(b)

**Figure 8.** (a) Partial regression plot; (b) comparison graph for actual and predicted values.

The *t*-test values assess the statistical significance of each coefficient. A larger absolute value for the *t*-test statistic indicates a stronger relationship between the dependent and independent variables. The *t*-test values for the actual value and incidence angle were 11.173 and  $-6.778$ , respectively. In this context, both variables are significant, but the higher *t*-test value for the actual value indicates its stronger correlation with the dependent variable than the incidence angle. The  $P > |T|$  values represent the probability of observing a *t*-test statistic as extreme as or more extreme than the observed value if the null hypothesis (which states that the coefficient is zero) were true.  $P > |T|$  values  $< 0.05$  are typically considered statistically significant. In this case, a value of zero obtained for both variables strongly rejects the null hypothesis, confirming that the incidence angle and actual value are statistically significant predictors of the dependent variable.

Thus, these values are essential for evaluating the validity and strength of the relationships between the dependent variable and each independent variable in the model. Furthermore, they aid in understanding the direction of these relationships (positive or negative) and their statistical significance and the reliability of the findings. In the next section, we will discuss the differences from previous studies and limitations of the study based on the results of this study.

## 4. Discussion

### 4.1. TIR Measured Temperature Discussion

The basic principle of a TIR camera relies on the energy and wavelengths emitted from a black body, making accurate temperature measurement the core of this technology. In this study, we calculated the mean values of data obtained from a total of 179 TIR images at 18 different locations. These results enhance the reliability of the TIR temperature values, as the study was conducted on six hotspot areas with varying temperature values as well as surrounding normal modules. This approach allowed us to increase the data reliability through a diverse distribution of temperatures, rather than limiting the analysis to a single temperature range. However, acquiring TIR data without considering the angle of incidence can lead to unreliable temperature values, causing confusion in detecting and managing faults in solar power plants.

Theoretically, according to Lambert's cosine law, when the angle of incidence is  $0^\circ$ , the emitted radiant energy directly reaches the camera, enabling the highest temperature measurement. Due to the  $20^\circ$  inclination of solar power plants, the angles of incidence for a3, b3, and c3 are close to  $0^\circ$ , resulting in the lowest angles of incidence (Table 8). This study anticipated that temperatures would be overestimated as the angle of incidence approached  $0^\circ$  and underestimated with higher angles of incidence. However, as mentioned in the results section, the highest temperature values did not come from the minimum angle of incidence positions a3, b3, and c3; rather, they were observed at a2, b2, and c2. This discrepancy implies that measured temperature values may differ from the actual temperatures of the targets due to scattering or absorbed radiant energy under real environmental conditions. Additionally, this indicates that the results may differ from the theory due to the STA of the solar panels located in the research area.

To address the issue of TIR data showing temperatures over  $13^\circ\text{C}$  higher than LST values, we propose leveraging the characteristic of reduced radiant energy intake as the angle of incidence increases to mitigate the overestimation of TIR temperature measurements. The objective of this study is not to detect hotspots but to propose effective measures for the periodic management of solar power plants.

Initial suspected hotspot areas are considered when there is a temperature difference of  $6\text{--}10^\circ\text{C}$  compared to normal modules. However, if temperatures are overestimated in non-hotspot areas, it could lead to significant confusion in managing and inspecting solar power plants. Therefore, acquiring TIR data considering the angle of incidence is crucial. Incorporating the angle of incidence into the existing research methodologies allows for consideration of both the thermal sensor and the target, which is expected to significantly contribute to the optimal acquisition of TIR data. The obtained TIR data were

collected on 11 October 2023, at 3:22 PM, in a warm environment with a temperature of 22.2 °C and humidity of 48%, at an approximate latitude of 36° in the Northern Hemisphere. The TIR data captured at 22.2 °C exhibited a considerable difference from LST data, with hotspots showing greater deviations compared to normal modules. The influence of the angle of incidence is expected to be more significant when capturing data in high-temperature environments.

**Table 8.** Incident angle between hotspot module and TIR camera.

Position of UAV	Number 1 Angle of Incidence	Number 2 Angle of Incidence	Number 3 Angle of Incidence	Number 4 Angle of Incidence	Number 5 Angle of Incidence	Number 6 Angle of Incidence
a1	16.72°	18.63°	15.47°	17.09°	15.22°	17.90°
a2	6.98°	6.16°	5.91°	8.35°	7.89°	10.24°
a3	2.78°	3.06°	2.66°	4.20°	6.97°	6.99°
a4	10.0°	10.71°	10.94°	10.45°	13.52°	11.85°
a5	19.41°	20.12°	20.40°	19.41°	22.30°	20.12°
a6	25.68°	23.72°	26.69°	25.53°	28.36°	26.04°
b1	22.89°	19.33°	19.70°	24.10°	16.86°	18.21°
b2	14.33°	9.75°	10.75°	7.17°	7.64°	9.09°
b3	8.35°	8.13°	4.51°	7.81°	0.91°	1.29°
b4	7.86°	12.80°	7.77°	5.33°	9.34°	8.16°
b5	13.87°	20.46°	15.95°	12.12°	11.53°	16.77°
b6	20.86°	27.09°	22.82°	18.76°	25.01°	25.68°
c1	32.21°	22.58°	25.95°	17.89°	19.13°	18.61°
c2	23.94°	16.09°	17.65°	11.22°	10.55°	9.85°
c3	17.09°	13.57°	11.38°	10.42°	5.58°	4.60°
c4	11.22°	15.98°	8.37°	14.48°	9.19°	9.03°
c5	10.82°	21.85°	12.74°	21.38°	16.73°	16.79°
c6	14.92°	28.44°	19.28°	28.57°	24.38°	24.55°

Given these considerations, future research aims to gather data during the peak temperatures of July and August to delve deeper into effective strategies for detecting and addressing defects in solar power plants. Furthermore, to overcome the challenge of obtaining the highest temperature measurements at the minimum angle of incidence, additional captures will be conducted at various times throughout the same day, taking into account the sun's position. This approach is expected to contribute to the acquisition of optimal TIR data.

Furthermore, due to the challenges associated with studying actual hotspot areas in real environments, this research employed a controlled setup using pre-heated silicone rubber pads to simulate hotspot regions. The material chosen closely mimicked the emissivity of the solar panels to create a scenario with temperature differentials of 6–10 °C above normal modules. However, it is acknowledged that this simulation may not fully capture the intricate characteristics of genuine hotspot areas, and the results in actual hotspot conditions may differ. This acknowledgment sets the stage for future studies, which will aim to conduct research based on actual hotspot areas to explore the discrepancies between the simulated outcomes presented in this study and real-world data. Further investigations will continuously be undertaken to analyze any differences that arise from such comparisons.

#### 4.2. Multiple Regression Analysis Discussion

Table 4 employs the Omnibus statistic to assess the normal distribution of residuals in regression analysis, a crucial test for one of the model's foundational assumptions: residual normality. However, the Omnibus value of 0.827 does not strongly support the normality of residuals. While a low Omnibus value typically indicates closer adherence to a normal

distribution, here it yields inconclusive results. Similarly, a PROB(Omnibus) value of 0.661 implies insufficient evidence to reject the hypothesis of residual normality. Despite  $p$ -values below 0.05 usually indicating statistical significance, the high  $p$ -value in this context does not robustly support residual normality. Consequently, while both Omnibus and PROB(Omnibus) values assess residual normality, they do not strongly confirm it and are insufficient to conclude significant deviation from normality.

The independence of residuals in regression analysis is evaluated through the Durbin–Watson statistic, testing for autocorrelation among residuals, another critical model assumption. A Durbin–Watson value of 1.321 suggests slight positive autocorrelation among residuals, falling between 1.5 and 2.5, indicating neither complete independence nor significant autocorrelation.

Skewness measures symmetry in residual distribution, crucial for assessing normality. A skewness value of 0.111 suggests relative symmetry, while kurtosis, measuring peak value, indicates minimal deviation from normality with a value of 2.609. However, the Jarque–Bera test does not strongly support normality, with a JB value of 0.909 and PROB(JB) value of 0.635, providing inconclusive evidence against non-normality.

Figure 9 illustrates that while the residuals of ‘incidence angle’ exhibit a random distribution, those of ‘actual values’ reveal a distinct pattern due to the discretization in data collection and processing. The irregularities observed in the histogram and minor deviations in the Q-Q plot may indicate the presence of outliers, significant data points, or nonlinear relationships that have not been modeled.

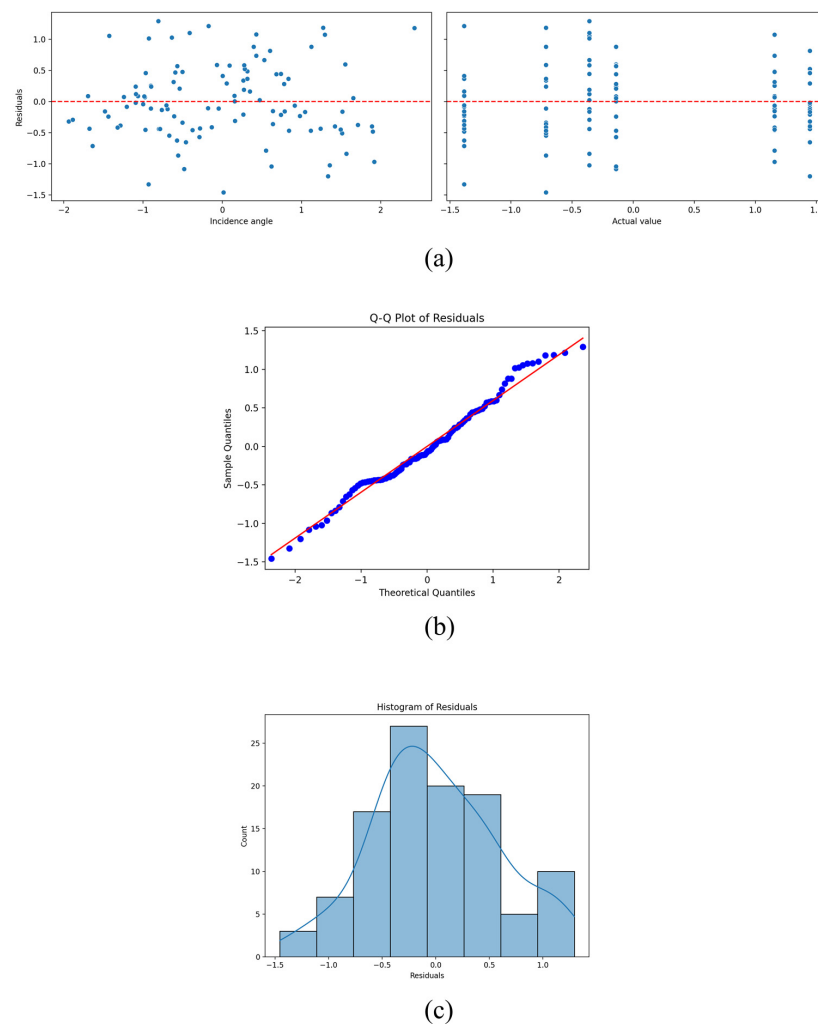


**Figure 9.** (a) Residual distribution plot of the incidence angle and actual value; (b) Q-Q residual plots; and (c) histogram of residuals.

To address these issues, it is imperative in future research to meticulously examine the data collection and processing methods for ‘actual values’ to ensure compatibility with regression analysis. Depending on the characteristics of the data, it may be necessary to apply appropriate statistical models such as Poisson regression or to reassess the handling methods for continuous variables. If feasible, collecting more detailed data to increase the accuracy of the actual measurements and adjust residuals could enhance the precision of the data. Furthermore, experimental studies conducted in actual hotspot environments based on the hypotheses of this study are expected to yield more accurate and reliable outcomes. The process of obtaining more precise regression results will provide definitive evidence supporting the importance of the incidence angle.

## 5. Conclusions

The conclusions of this study emphasize the importance of adjusting the angle of incidence to minimize external influences and enhance the accuracy of surface temperature measurements. When TIR data from 18 different angles of incidence were collected for both normal and hotspot modules, varying temperature values were extracted at different angles. This result suggests that while the relationship between the thermal sensor and zenith angle has been the focus of previous research, the variation in the angle of incidence between the thermal sensor, the research area, and the target objects must also be considered when acquiring TIR data. Notably, the positions at a6, b6, and c6 showed the smallest temperature differences, indicating that these angles may be optimal. However, it cannot be definitively concluded that these angles increase the accuracy of hotspot module detection. The research was conducted with a set temperature difference of approximately 10 °C between randomly established hotspots and standard modules, and this difference persisted throughout the study. Nonetheless, acquiring TIR data at locations with angles of incidence over 20° has shown a reduction in the temperature difference between hotspots and standard modules. This reduction could potentially lead to misidentification of actual hotspot areas as normal modules, despite these having the closest temperature values to the LST, thus potentially impeding early detection of hotspot modules.

Therefore, when the angle of incidence between the UAV-based TIR camera and the hotspot modules is within the range of 15–20°, it yields the most accurate TIR temperature measurements and demonstrates exceptional temperature precision. Consequently, lower angles of incidence are likely to produce temperature readings that exceed the LST values. Implementing a strategy to capture TIR data considering an angle of incidence within this range is expected to enhance the precision in detecting the temperature of solar panels and contribute to the accurate identification of suspected initial hotspot areas. Accurate detection of such areas in solar power plants can significantly reduce maintenance and manpower costs, increase energy efficiency, and extend the lifespan of solar panels, thereby providing numerous benefits across various aspects of solar power facility operations.

**Author Contributions:** Conceptualization, H.S. and K.K.; methodology, H.S. and W.L.; software, H.S. and K.L.; formal analysis, H.S. and K.K.; investigation, S.J. and D.K.; resources, H.S. and K.L.; writing—original draft preparation, H.S.; writing—review and editing, W.L.; visualization, H.S.; supervision, W.L.; funding acquisition, W.L. All authors have read and agreed to the published version of the manuscript.

**Funding:** This work was partly supported by the Korea Institute of Energy Technology Evaluation and Planning (KETEP) grant funded by the Korea government (MOTIE) (20224000000290, Global Training Program of Human Resource for Smart Energy System) and the National Research Foundation of Korea (NRF) grant funded by the Korea government (MSIT) (NRF-2021R1A5A8033165).

**Data Availability Statement:** The raw data supporting the conclusions of this article will be made available by the authors on request.

**Acknowledgments:** The authors wish to acknowledge the Research Institute of Artificial Intelligent Diagnosis Technology for Multi-scale Organic and Inorganic Structure, Kyungpook National University, Sangju, Republic of Korea, for providing laboratory facilities.

**Conflicts of Interest:** The authors declare no conflicts of interest.

## References

1. IEA. Renewable Energy Market Update: Outlook for 2021 and 2022. Available online: <https://iea.blob.core.windows.net/assets/18a6041d-bf13-4667-a4c2-8fc008974008/RenewableEnergyMarketUpdate-Outlookfor2021and2022.pdf> (accessed on 12 December 2023).
2. Makrides, G.; Zinsser, B.; Schubert, M.; Georghiou, G.E. Performance loss rate of twelve photovoltaic technologies under field conditions using statistical techniques. *Sol. Energy* **2014**, *103*, 28–42. [CrossRef]
3. Kim, J.; Rabelo, M.; Padi, S.P.; Yousuf, H.; Cho, E.C.; Yi, J. A Review of the Degradation of Photovoltaic Modules for Life Expectancy. *Energies* **2021**, *14*, 4278. [CrossRef]
4. Rahaman, S.A.; Urmee, T.; Parlevliet, D.A. PV system defects identification using Remotely Piloted Aircraft (RPA) based infrared (IR) imaging: A review. *Sol. Energy* **2020**, *206*, 579–595. [CrossRef]
5. Dalsass, M.; Scheuerpflug, H.; Maier, M.; Brabec, C.J. Correlation between the monitoring data of a photovoltaic power plant and module defects detected by drone-mounted thermography. In Proceedings of the 2016 IEEE 43rd Photovoltaic Specialists Conference (PVSC), Portland, OR, USA, 14–18 September 2015; pp. 14–18.
6. Köntges, M.; Kurtz, S.; Packard, C.E.; Jahn, U.; Berger, K.A.; Kato, K.; Friesen, T.; Liu, H.; Van Iseghem, M.; Wohlgemuth, J.; et al. *Review of Failures of Photovoltaic Modules*; IEA International Energy Agency: Paris, France, 2014.
7. Dunlop, E.D.; Halton, D.; Ossenbrink, H.A. 20 years of life and more: Where is the end of life of a PV module? In Proceedings of the Conference Record of the Thirty-First IEEE Photovoltaic Specialists Conference, 2005, Lake Buena Vista, FL, USA, 3–7 January 2005; pp. 1593–1596.
8. Buerhop, C.; Schlegel, D.; Niess, M.; Vodermaier, C.; Weißmann, R.; Brabec, C.J. Reliability of IR-imaging of PV-plants under operating conditions. *Sol. Energy Mater. Sol. Cells* **2012**, *107*, 154–164. [CrossRef]
9. Käsiewieter, J.; Haase, F.; Larrodé, M.H.; Köntges, M. Cracks in solar cell metallization leading to module power loss under mechanical loads. *Energy Procedia* **2014**, *55*, 469–477. [CrossRef]
10. Usamentiaga, R.; Venegas, P.; Guerediaga, J.; Vega, L.; Molleda, J.; Bulnes, F.G. Infrared thermography for temperature measurement and non-destructive testing. *Sensors* **2014**, *14*, 12305–12348. [CrossRef] [PubMed]
11. Salazar, A.M.; Macabebe, E.Q.B. Hotspots detection in photovoltaic modules using infrared thermography. In Proceedings of the MATEC Web of Conferences, Les Ulis, France, 25–27 May 2016; p. 10015.
12. Acciani, G.; Simione, G.B.; Vergura, S. Thermographic analysis of photovoltaic panels. In Proceedings of the International Conference on Renewable Energies and Power Quality (ICREPQ'10), Granada, Spain, 23–25 March 2010; pp. 23–25.
13. Muntwyler, U.; Schuepbach, E.; Lanz, M. Infrared (IR) drone for quick and cheap PV inspection. In Proceedings of the 31st European Photovoltaic Solar Energy Conference and Exhibition, Hamburg, Germany, 14–18 September 2015; pp. 1804–1806.
14. Gallardo-Saavedra, S.; Hernández-Callejo, L.; Duque-Perez, O. Technological review of the instrumentation used in aerial thermographic inspection of photovoltaic plants. *Renew. Sustain. Energy Rev.* **2018**, *93*, 566–579. [CrossRef]
15. Kim, D.; Youn, J.; Kim, C. Automatic photovoltaic panel area extraction from UAV thermal infrared images. *J. Korean Soc. Surv. Geod. Photogramm. Cartogr.* **2016**, *34*, 559–568. [CrossRef]
16. Zefri, Y.; ElKettani, A.; Sebari, I.; Ait Lamallam, S. Thermal infrared and visual inspection of photovoltaic installations by UAV photogrammetry—Application case: Morocco. *Drones* **2018**, *2*, 41. [CrossRef]
17. de Oliveira, A.K.V.; Aghaei, M.; Rüther, R. Aerial infrared thermography for low-cost and fast fault detection in utility-scale PV power plants. *Sol. Energy* **2020**, *211*, 712–724. [CrossRef]
18. Álvarez-Tey, G.; Jiménez-Castañeda, R.; Carpio, J. Analysis of the configuration and the location of thermographic equipment for the inspection in photovoltaic systems. *Infrared Phys. Technol.* **2017**, *87*, 40–46. [CrossRef]
19. Moretón, R.; Lorenzo, E.; Narvarte, L. Experimental observations on hot-spots and derived acceptance/rejection criteria. *Sol. Energy* **2015**, *118*, 28–40. [CrossRef]
20. Moretón, R.; Lorenzo, E.; Leloux, J.; Carrillo, J.M. Dealing in practice with hot-spots. In Proceedings of the 29th European Photovoltaic Solar Energy Conference and Exhibition, Amsterdam, The Netherlands, 22–26 September 2014; pp. 1–6.
21. Tsanakas, J.A.; Ha, L.; Buerhop, C. Faults and infrared thermographic diagnosis in operating c-Si photovoltaic modules: A review of research and future challenges. *Renew. Sustain. Energy Rev.* **2016**, *62*, 695–709. [CrossRef]
22. Tanda, G.; Migliazzi, M. Infrared thermography monitoring of solar photovoltaic systems: A comparison between UAV and aircraft remote sensing platforms. *Therm. Sci. Eng. Prog.* **2024**, *48*, 102379. [CrossRef]
23. Kandeal, A.W.; Elkadeem, M.R.; Thakur, A.K.; Abdelaziz, G.B.; Sathyamurthy, R.; Kabeel, A.E.; Yang, N.; Sharshir, S.W. Infrared thermography-based condition monitoring of solar photovoltaic systems: A mini review of recent advances. *Sol. Energy* **2021**, *223*, 33–43. [CrossRef]
24. Buerhop, C.; Pickel, T.; Dalsass, M.; Scheuerpflug, H.; Camus, C.; Brabec, C.J. aIR-PV-check: A quality inspection of PV-power plants without operation interruption. In Proceedings of the 2016 IEEE 43rd Photovoltaic Specialists Conference (PVSC), Portland, OR, USA, 5–10 June 2016; pp. 1677–1681.
25. Aghaei, M.; Leva, S.; Grimaccia, F. PV power plant inspection by image mosaicing techniques for IR real-time images. In Proceedings of the 2016 IEEE 43rd Photovoltaic Specialists Conference (PVSC), Portland, OR, USA, 5–10 June 2016; pp. 3100–3105.

26. Leva, S.; Aghaei, M.; Grimaccia, F. PV power plant inspection by UAS: Correlation between altitude and detection of defects on PV modules. In Proceedings of the 2015 IEEE 15th International Conference on Environment and Electrical Engineering (EEEIC), Rome, Italy, 10–13 June 2015; pp. 1921–1926.
27. Quater, P.B.; Grimaccia, F.; Leva, S.; Mussetta, M.; Aghaei, M. Light Unmanned Aerial Vehicles (UAVs) for cooperative inspection of PV plants. *IEEE J. Photovolt.* **2014**, *4*, 1107–1113. [[CrossRef](#)]
28. Rahaman, S.A.; Urmee, T.; Parlevliet, D.A. Investigate the impact of environmental and operating conditions of infrared (IR) imaging on infrared thermography of PV modules to identify defects. *Sol. Energy* **2022**, *245*, 231–253. [[CrossRef](#)]
29. Lagouarde, J.; Hénon, A.; Kurz, B.; Moreau, P.; Irvine, M.; Voogt, J.; Mestayer, P. Modelling Daytime Thermal Infrared Directional Anisotropy over Toulouse City Centre. *Remote Sens. Environ.* **2010**, *114*, 87–105. [[CrossRef](#)]
30. Lagouarde, J.; Dayau, S.; Moreau, P.; Guyon, D. Directional Anisotropy of Brightness Surface Temperature over Vineyards: Case Study over the Medoc Region (SW France). *IEEE Geosci. Remote Sens. Lett.* **2013**, *11*, 574–578. [[CrossRef](#)]
31. Bian, Z.; Roujean, J.; Lagouarde, J.; Cao, B.; Li, H.; Du, Y.; Liu, Q.; Xiao, Q.; Liu, Q. A Semi-Empirical Approach for Modeling the Vegetation Thermal Infrared Directional Anisotropy of Canopies Based on using Vegetation Indices. *ISPRS J. Photogramm. Remote Sens.* **2020**, *160*, 136–148. [[CrossRef](#)]
32. Bian, Z.; Roujean, J.; Cao, B.; Du, Y.; Li, H.; Gamet, P.; Fang, J.; Xiao, Q.; Liu, Q. Modeling the Directional Anisotropy of Fine-Scale TIR Emissions over Tree and Crop Canopies Based on UAV Measurements. *Remote Sens. Environ.* **2021**, *252*, 112150. [[CrossRef](#)]
33. Kimes, D.S.; Kirchner, J.A. Directional Radiometric Measurements of Row-Crop Temperatures. *Int. J. Remote Sens.* **1983**, *4*, 299–311. [[CrossRef](#)]
34. Hu, L.; Monaghan, A.; Voogt, J.A.; Barlage, M. A First Satellite-Based Observational Assessment of Urban Thermal Anisotropy. *Remote Sens. Environ.* **2016**, *181*, 111–121. [[CrossRef](#)]
35. Trigo, I.F.; Monteiro, I.T.; Olesen, F.; Kabsch, E. An Assessment of Remotely Sensed Land Surface Temperature. *J. Geophys. Res. Atmos.* **2008**, *113*, D17108. [[CrossRef](#)]
36. DJI Science and Technology Co., Ltd. Zenmuse\_H20\_Series\_User\_Manual-EN v1.0, 05, Shenzhen, China. 2020. Available online: [https://dl.djicdn.com/downloads/Zenmuse\\_H20\\_Series/Zenmuse\\_H20\\_Series\\_User\\_Manual-EN.pdf](https://dl.djicdn.com/downloads/Zenmuse_H20_Series/Zenmuse_H20_Series_User_Manual-EN.pdf) (accessed on 6 December 2023).
37. Benetech products Co., Ltd. Benetech\_GM320-EN-01, 06, Shenzhen, China. 2015. Available online: [https://supermagneter.no/pub/media/downloads/manuals/Benetech\\_GM320.pdf](https://supermagneter.no/pub/media/downloads/manuals/Benetech_GM320.pdf) (accessed on 6 December 2023).
38. Lee, K.; Lee, W.H. Temperature Accuracy Analysis by Land Cover According to the Angle of the Thermal Infrared Imaging Camera for Unmanned Aerial Vehicles. *ISPRS Int. J. Geo-Inf.* **2022**, *11*, 204. [[CrossRef](#)]
39. Elsobeiey, M.E. Accuracy assessment of satellite-based correction service and virtual GNSS reference station for hydrographic surveying. *J. Mar. Sci. Eng.* **2020**, *8*, 542. [[CrossRef](#)]

**Disclaimer/Publisher’s Note:** The statements, opinions and data contained in all publications are solely those of the individual author(s) and contributor(s) and not of MDPI and/or the editor(s). MDPI and/or the editor(s) disclaim responsibility for any injury to people or property resulting from any ideas, methods, instructions or products referred to in the content.